Power spectrum of resting-state blood-oxygen-level-dependent signal

J. C. Pang[1,2,3,*] and P. A. Robinson[1,2]
[1]*School of Physics, University of Sydney, Sydney, NSW 2006, Australia*
[2]*Center for Integrative Brain Function, University of Sydney, Sydney, NSW 2006, Australia*
[3]*QIMR Berghofer Medical Research Institute, Herston, QLD 4006, Australia*

(Received 22 October 2018; revised manuscript received 22 July 2019; published 29 August 2019)

Hemodynamic modeling is used to explore the origin, predict, and analyze the power spectrum of the resting-state blood-oxygen-level-dependent (BOLD) signal measured by functional magnetic resonance imaging (fMRI), which has been reported to have a power-law form, i.e., $P(f) \propto f^{-s}$, where $P(f)$ is the power, f is the frequency, and $s > 0$ is the power-law exponent. However, current fMRI experimental paradigms have limited acquisition durations, affecting the spectral resolution of fMRI data at the low-frequency regime. Here, the claimed power-law spectrum is investigated by using a recent hemodynamic model to analytically derive the BOLD power spectrum, with parameters that are related to neurophysiology. The theoretical results show that, for all realistic parameter combinations, the BOLD power spectrum is flat at $f \lesssim 0.01$ Hz, has a weak resonance originating from intrinsic oscillations of vasodilatory response, and becomes a power law for high frequencies, all of which is in agreement with an empirical data set that describes the spectrum of one subject and brain region. However, the results are contrary to studies reporting a pure power-law spectrum at $f \lesssim 0.2$ Hz. The discrepancy is attributed largely to data averaging employed by current approaches that averages together important properties of the BOLD power spectrum, such as its resonance, that biases the spectrum to only show a power law. Data averaging also reduces the high-frequency power-law exponent relative to individual cases. Overall, this work demonstrates how the model can reproduce BOLD dynamics and further analyze its low-frequency behavior. Moreover, it also uses the model to explain the impact of procedures, such as data averaging, on the reported features of the BOLD power spectrum.

DOI: 10.1103/PhysRevE.100.022418

I. INTRODUCTION

Functional magnetic resonance imaging (fMRI) indirectly detects brain activity through changes in oxygenation that accompany it, based on measuring the blood-oxygen-level-dependent (BOLD) signal [1]. Due to its high spatial resolution, fMRI has led to substantial advances in understanding brain organization by revealing brain regions activated during behavioral manipulations (see the review in Ref. [2]). It was initially believed that signal fluctuations unrelated to the manipulation are driven largely by noise and do not provide useful information. However, the pioneering work of Biswal *et al.* changed this paradigm by demonstrating that, in the absence of an experimenter-imposed task when a subject lies quietly in the scanner (commonly referred to as the "resting state," although the brain is still active), spontaneous BOLD signals are highly correlated among functionally related brain regions [3]. This finding has driven interesting new avenues of neuroimaging research, including investigations of the functional topography of the brain, signal variability in evoked responses, and abnormal intrinsic activity of the diseased brain [4–6].

Power spectral analysis, which characterizes the energy distribution of a signal with respect to frequency, reveals that spontaneous BOLD fluctuations predominantly occur at low frequencies, with significant power only at frequencies $\lesssim$0.2 Hz because of slow cerebrovascular responses [7–10]. The significance of these low-frequency fluctuations is not fully understood but several findings suggest that they may account for endogenous functional connectivity fluctuations, autoregulatory vasomotion, intracellular calcium signaling, or uncontrolled cognitive processes [9–13]. In order to properly understand these BOLD fluctuations, it is important to characterize the relevant power spectrum.

Several studies have reported that the power spectrum of spontaneous BOLD follows a power law $P(f) \propto f^{-s}$ in the limit of small frequencies ($f \to 0$), which is indicative of scale-free properties [14], where $P(f)$ is the power, f is the frequency, and $s > 0$ is the power-law exponent [7,15–19], with large s indicating long-range memory [20] and small s suggesting efficient information processing [17,21]. It has also been reported that the exponent s differs between brain regions [typically in the range 0–3, which is demonstrated by the empirical data in Fig. 1(a)] and during task activation [17]. However, the precise mechanisms that lead to the emergence of the power-law spectrum and differences in the reported power-law exponents remain unclear.

Even though a power-law BOLD spectrum has been widely reported, there are still several issues that need to be systematically addressed to verify its existence and better understand the low-frequency dynamics of BOLD and their relation to physiology. First, current studies typically

*Corresponding author: james.pang@qimrberghofer.edu.au, james.pang@sydney.edu.au

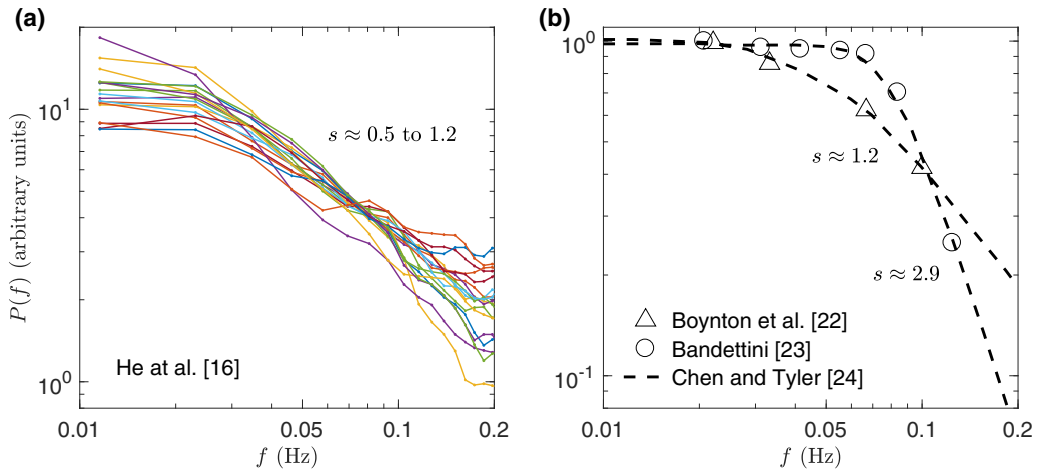

FIG. 1. Scanned and digitized BOLD power spectrum data. (a) Data for 18 cortical regions from Ref. [16]. Each curve is an average of spectra from 17 subjects. (b) Data for the visual cortex (triangles) from Ref. [22], for the motor cortex (circles) from Ref. [23], and their corresponding second-order low-pass filter fits (dashed lines) from Ref. [24]. The approximate power-law exponents (s) of the asymptotic curves are also shown, with $P(f) \propto f^{-s}$.

investigate the BOLD power spectrum at the frequency range $0.01\ \text{Hz} \leqslant f \leqslant 0.2\ \text{Hz}$, as shown in Fig. 1, covering only around one decade in frequency. Observation over such a limited range is insufficient to conclude with certainty that the data follow a power law and not some alternative distribution such as a lognormal or stretched exponential [25,26]. Second, it is also not known whether BOLD continues to exhibit a power-law spectrum at $f \lesssim 0.01$ Hz [4] because experimental paradigms with longer acquisition durations are necessary to investigate this frequency range. Also, since a power law would diverge as $f \to 0$, there must be a lower bound f_{min} such that a power-law spectrum ceases to exist at $f < f_{\text{min}}$. In fact, empirical and theoretical works have suggested that the BOLD power spectrum is flat at $f \lesssim 0.02$ Hz and transitions to a power law at $f \gtrsim 0.08$ Hz, as shown in Fig. 1(b) [22–24]. Third, our previous theoretical studies demonstrated that the hemodynamic response resonates weakly at about 0.07 Hz, originating from intrinsic oscillations of the vasodilatory response [8,27], which is not reported in most studies because of insufficient frequency resolution. Certainly, a pure power-law spectrum cannot account for the existence of this resonance. Fourth, analyses of low-frequency BOLD often require interpolation of poorly resolved data or multivoxel/multisubject averaging to increase the signal-to-noise ratio. These introduce statistical artifacts that inevitably change the behavior of the data, which result in power spectra that may or may not represent the true underlying mechanisms of the data [25]. Finally, fMRI data analysis is susceptible to non-neuronal noise components, including physiological fluctuations, thermal noise, and scanner noise, that can inevitably influence the resulting BOLD power spectrum [28].

In this paper, we address the above concerns by analytically deriving the BOLD power spectrum using a physiological cortical hemodynamic model, which can accurately predict the neurally driven BOLD signal via its hemodynamic mechanisms [27,29–33]. The advantage of using the model is that the derived BOLD power spectrum is independent of experimental artifacts, data preprocessing effects, and other physiological confounds; thus, its low-frequency behavior can be better analyzed, resolving issues in current fMRI spectral studies. Furthermore, the model involves parameters that are related to neurophysiology, hence it can reflect the intrinsic variability of properties of different brain regions and different subjects and can be used to explain the impact of data averaging performed by current approaches on the reported features of the BOLD power spectrum.

II. CORTICAL HEMODYNAMIC MODEL

BOLD fMRI has been used in a wide variety of studies, leading to significant insights into brain activation and function. To better understand the physical principles underlying BOLD, physically based mathematical models play an important role because they can unify a multitude of properties and can systematically describe the dynamics in terms of physiologically realistic parameters, resulting in predictions that can guide further experimental explorations.

In this section, we outline the principles and processes of a recent cortical hemodynamic model that can represent BOLD dynamics. Then, we describe the resulting transfer function from the model that predicts the BOLD response to an arbitrary neural stimulus. This transfer function is crucial for determining the analytic BOLD power spectrum in Sec. III; our previous articles contain detailed discussions and derivations [29–31,33].

A. Principles and processes

The hemodynamic model incorporates properties of cortical tissue and quantifies dynamics using a physical approach governed by the following principles.

The cortical vasculature is organized to efficiently transport blood from arteries to veins throughout the cortex. First, the cortical surface is covered by pial arteries and pial veins. Then, pial arteries connect to intracortical arteries that penetrate the cortical tissue perpendicular to the surface and branch out into smaller segments, i.e., arterioles and capillaries. Finally, the capillaries merge into venules and intracortical veins

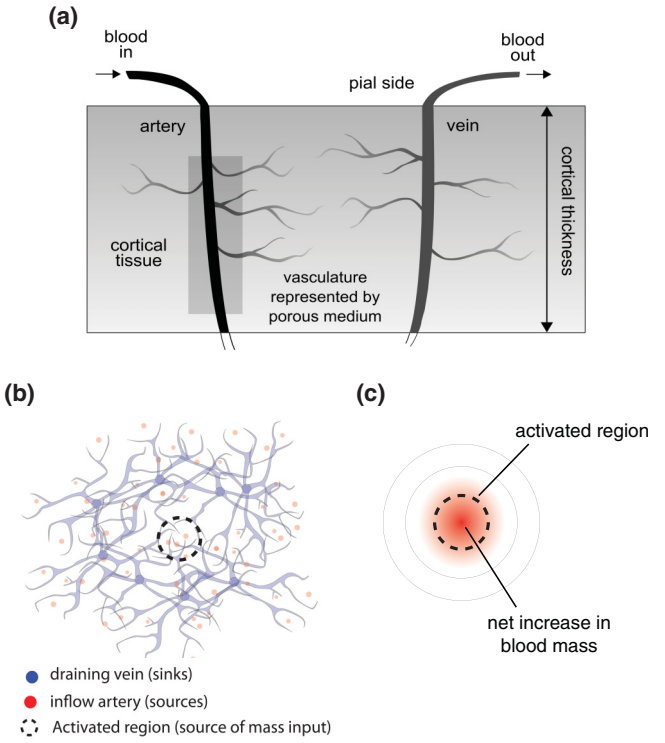

FIG. 2. Principles governing the cortical hemodynamic model. Images adapted from Refs. [29,30]. (a) Cortical tissue is approximated as a poroelastic medium showing an approximately vertical descending artery and ascending vein. (b) 2D cortical sheet showing various sources and sinks of blood mass. The dashed circle represents the activated region. (c) Details of vasculature are averaged out and dynamics are calculated as local averages (mean field).

that run parallel to the intracortical arteries, then ascend to the surface and join pial veins [34]. This structure of ascending and descending cortical vessels is the first principle that governs the model, allowing the cortical tissue to be approximated as a poroelastic medium where the vessels represent as the "pores" within an elastic matrix, as shown in Fig. 2(a).

Despite the heterogeneity of the vasculature across the layers of the cortex, Duvernoy and colleagues demonstrated that on the plane of the cortex, each intracortical vein is surrounded by a ring of intracortical arteries [34], with arteries outnumbering the veins approximately 5–10 to 1. The periodic architecture of arteries and veins and their perpendicular orientations with respect to the cortical surface allows the cortex to be modeled as a two-dimensional (2D) sheet that aggregates the properties of the vasculature over the cortical depth, as shown in Fig. 2(b). Finally, the model uses a mean-field approach, wherein the properties and dynamics of vessels are treated as local averages over scales $\gtrsim$0.5 mm, as shown in Fig. 2(c).

Using the above principles, the hemodynamic model can quantify spatiotemporal changes of neurovascular quantities that contribute to BOLD via coupled partial differential equations; the interactions of these quantities are shown in the block diagram in Fig. 3. Briefly, the model considers that neural activity activates nearby astrocytes. The astrocytes produce a response called the neuroglial drive, which affects the surrounding vasculature, leading to an increase in blood inflow. Forces between blood and tissue lead to inflation of the vasculature, similarly to the single-voxel temporal balloon model [35,36], thereby changing blood mass and volume in the activated region. Physical constraints, such as boundary conditions, spatial continuity, and conservation of blood mass and momentum, are then incorporated in the model to regulate the total changes in blood flow and volume. The resulting changes in blood flow and volume lead to variations in the ratio between the blood's oxygenated hemoglobin (oHb) and deoxygenated hemoglobin (dHb) concentrations. Finally, changes in blood volume and dHb concentration contribute to changes in BOLD via a BOLD signal equation [36]. Full details of the model and its mathematical formulation are provided in our previous publications [29–31,33].

The above model has successfully predicted propagating cortical hemodynamic waves in multiple fMRI experiments [30,37,38], which have been experimentally validated using other methods such as two-photon microscopy [39] and a data-driven model of effective connectivity [40]. These propagating waves have also been observed in a number of other recent studies [41,42]. The model has also been used to develop methods that can deconvolve the spatiotemporal variations of neurovascular signals that contribute to BOLD [33,43]. More importantly, the model rests on parameters that can be measured independently to reflect the physiology and hemodynamics of individual subjects and brain regions.

B. Transfer function

In our model, the neurovascular quantities obey dynamical equations that can be used to predict nonlinear hemodynamic responses to arbitrary neural activity. Experiments have shown that the hemodynamic response is approximately linear for a wide array of stimuli that induce low-amplitude responses [8,22,30,44]; hence, we can linearize the equations of the model, which allows their analysis in Fourier space [30,31].

Once the model equations are linearized and Fourier transformed, we can understand their properties at each spatial frequency $\mathbf{k}$ and temporal angular frequency ω. This leads to a

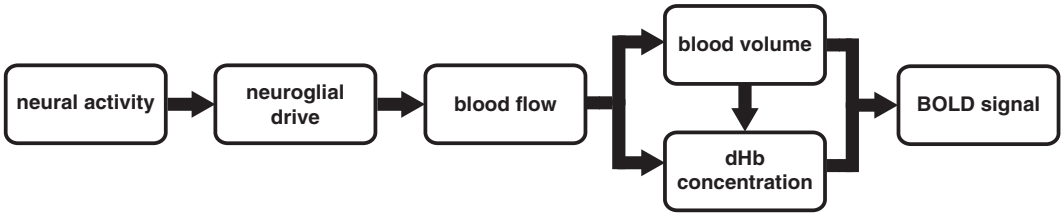

FIG. 3. Block diagram showing the major neurovascular quantities and their causal links considered in the hemodynamic model.

TABLE I. Physiological values of the model parameters [29–32,34,45–50]. In each row, the columns from left to right detail the parameter, its symbol or formula, its value or range, and its units, respectively.

Parameter	Symbol	Value/range	Units
Blood mass density	ρ_f	1062	kg m^{-3}
Mean elasticity exponent of cortical vessels	β	1.7–3.6	
Hemodynamic transit time	τ	1–4	s
Fractional oxygen consumption rate	η	0.4	s^{-1}
Resting blood volume fraction	V_0	0.03	
Magnetic field parameters at 3 T, TE = 30 ms	k_1, k_2, k_3	4.2, 1.7, 0.41	
Blood flow signal decay rate	κ	0.1–1	s^{-1}
Natural frequency of flow response	ω_f	0.1–1	s^{-1}
Mean cortical thickness	L	$(1–4.5)\times10^{-3}$	m
Astrocytic delay	τ_d	0.2–2.4	s
Wave propagation speed	v_β	$(1–12)\times10^{-3}$	m s^{-1}
Wave damping rate	Γ	0.1–1	s^{-1}
Perpendicular spatial frequency	$k_0 = \cos^{-1}(0.8)/L$	143–644	m^{-1}
Outflow normalization constant	$C_z = (1\times10^{-3}\ \text{m})\cdot k_0/[3\sin(k_0 L)]$	0.08–0.36	
Effective blood viscosity	$D = \rho_f(2\Gamma - \beta C_z/\tau)$	$(0.05–2.1)\times10^{3}$	kg m^{-3} s^{-1}
Effective spatial frequency	$k_z = \sqrt{k_0^2 + \frac{1}{v_\beta^2} C_z \frac{\beta}{\tau}\frac{D}{\rho_f}}$	$(0.14–1.7)\times10^{3}$	m^{-1}

set of transfer functions $T_{AB}(\mathbf{k},\omega)$ that describes the change in an arbitrary quantity A per unit change in an arbitrary quantity B at the same $\mathbf{k}$ and ω.

The most relevant transfer function for this study is $T_{Y\phi}$ that relates the BOLD signal Y to neural activity ϕ such that

$$Y(\mathbf{k},\omega) = T_{Y\phi}(\mathbf{k},\omega)\phi(\mathbf{k},\omega), \tag{1}$$

where $Y(\mathbf{k},\omega)$ and $\phi(\mathbf{k},\omega)$ are the Fourier transforms of the BOLD signal and the neural activity, respectively. Previous works showed that [27,30,31,33]

$$T_{Y\phi}(\mathbf{k},\omega) = \frac{A(\omega)}{\prod_{j=1}^{3} B_j(k,\omega)}, \tag{2}$$

where $|\mathbf{k}|^2 = k^2$ is the spatial wave number in the plane of the cortex,

$$A(\omega) = \left(i\omega^2 P + \omega Q + iR\right)\mathrm{e}^{-i\omega\tau_d}, \tag{3}$$

$$B_1(k,\omega) = k^2 v_\beta^2 + k_z^2 v_\beta^2 - \omega^2 - 2i\Gamma\omega, \tag{4}$$

$$B_2(k,\omega) = B_2(\omega) = -\left(\omega + \tfrac{1}{2}i\kappa\right)^2 + \omega_f^2, \tag{5}$$

$$B_3(k,\omega) = B_3(\omega) = \omega + i\eta + i\tau^{-1}, \tag{6}$$

and the real-valued constants P, Q, and R are

$$P = -C_z[k_2 - k_3 - V_0(k_1 + k_2)], \tag{7}$$

$$Q = C_z\left\{(k_2 - k_3)(\eta+\tau^{-1}) - (k_1 + k_2)C_z[\eta-\tau^{-1}(\beta - 2)] + \frac{D}{\rho_f}[k_2 - k_3 - V_0(k_1 + k_2)]\right\}, \tag{8}$$

$$R = C_z\frac{D}{\rho_f}\{(k_2 - k_3)(\eta + \tau^{-1}) - (k_1+k_2)C_z[\eta-\tau^{-1}(\beta-2)]\}. \tag{9}$$

Each $B_j(k,\omega)$ defines a dispersion relation whose solutions are independent BOLD response modes, which govern the fundamental patterns of oscillations of the BOLD signal [27]. In particular, $B_1(k,\omega)$, $B_2(k,\omega)$, and $B_3(k,\omega)$ are related to damped-wave, local-oscillating, and local-decaying BOLD response modes, respectively [27,33]. All the parameters in Eqs. (3)–(9) have a physiological significance that describes the properties of blood, vasculature, or the fMRI scanner. Table I details these parameters together with their physiological values or ranges that are either obtained from known estimates or derived from steady-state behavior [29–32,34,45–50]. Note that the dependent parameters k_0, C_z, D, and k_z need to remain positive and real valued, hence constraining the possible combinations of independent parameters.

III. THEORETICAL BOLD POWER SPECTRUM

In this section, we analytically derive the power spectrum of spontaneous BOLD via the transfer function in Eq. (2) using white noise as the input stimulus. Then, the power spectrum is approximated at low frequencies ($\omega \ll \omega_T$) and at high frequencies ($\omega \gg \omega_T$), where ω_T is a transition frequency that is determined below.

A. Power spectrum derivation

The temporal BOLD power spectrum $P_{\mathrm{BOLD}}(\omega)$ can be derived by integrating the squared magnitude of $Y(\mathbf{k},\omega)$ with respect to the spatial frequency vector $\mathbf{k}$, i.e.,

$$P_{\mathrm{BOLD}}(\omega) = \frac{1}{(2\pi)^2}\int_{-\infty}^{\infty}|Y(\mathbf{k},\omega)|^2\, d^2\mathbf{k} = \frac{1}{2\pi}\int_0^{\infty}|Y(\mathbf{k},\omega)|^2 k\, dk. \tag{10}$$

Upon substituting Eq. (1) into Eq. (10), we get

$$P_{\mathrm{BOLD}}(\omega) = \frac{1}{2\pi}\int_0^\infty |T_{Y\phi}(\mathbf{k},\omega)|^2 |\phi(\mathbf{k},\omega)|^2 k\, dk. \tag{11}$$

Equation (11) allows us to calculate the power spectrum of BOLD for any input neural activity ϕ. Several studies have shown that fluctuations in the resting-state BOLD signal are positively correlated with those in the power of low-frequency electroencephalography (EEG) oscillations ($f < 4$ Hz) [51,52], demonstrating that the low-frequency EEG power directly affects both the amplitude and power of the BOLD signal. Experimental and theoretical works have also shown that the shape of the resting-state EEG spectrum is approximately flat at $f < 1$ Hz [53–55]. Since BOLD is only significant below the cutoff frequency ≈0.2 Hz, as mentioned in the Introduction, the spectral profile of the neural activity ϕ in Eq. (11) can be approximated to be flat such that $|\phi(\mathbf{k},\omega)|^2 = \text{const}$ (≈1 for simplicity). This effectively assumes that the neural activity is an uncorrelated white noise driven by internal fluctuations from the cortical or subcortical regions (e.g., brain stem). This assumption has been successfully used in different neural models to predict cortical dynamics that match empirical data [56,57]. However, the effects of other potential forms of the noise spectrum, specifically of the power-law form f^γ [58], are further explored in Sec. VI.

Substituting Eq. (2) into Eq. (11) for the $|\phi(\mathbf{k},\omega)|^2 = 1$ unit, without loss of generality, we obtain

$$P_{\mathrm{BOLD}}(\omega) = \frac{1}{2\pi}\int_0^\infty \frac{|A(\omega)|^2 k\, dk}{\prod_{j=1}^3 |B_j(k,\omega)|^2}. \tag{12}$$

Note that $A(\omega)$, $B_2(k,\omega) = B_2(\omega)$, and $B_3(k,\omega) = B_3(\omega)$ are independent of k. Hence, we can simplify the integral to

$$P_{\mathrm{BOLD}}(\omega) = \frac{1}{2\pi}\frac{|A(\omega)|^2}{|B_2(\omega)|^2|B_3(\omega)|^2}\int_0^\infty \frac{k\, dk}{|B_1(k,\omega)|^2}. \tag{13}$$

Substitution of Eqs. (3)–(6) into Eq. (13) yields

$$P_{\mathrm{BOLD}}(\omega) = \frac{1}{2\pi}\frac{P^2\omega^4 + (Q^2+2PR)\omega^2 + R^2}{\left[\left(-\omega^2 + \frac{1}{4}\kappa^2 + \omega_f^2\right)^2 + \kappa^2\omega^2\right][\omega^2 + (\eta+\tau^{-1})^2]}\int_0^\infty \frac{k\, dk}{\left(k^2v_\beta^2 + k_z^2v_\beta^2 - \omega^2\right)^2 + 4\Gamma^2\omega^2}. \tag{14}$$

Letting $u = k^2v_\beta^2 + k_z^2v_\beta^2 - \omega^2$, the integral can be evaluated as

$$I = \frac{1}{2v_\beta^2}\int_{k_z^2v_\beta^2-\omega^2}^\infty \frac{du}{u^2 + 4\Gamma^2\omega^2} \tag{15}$$

$$= \frac{1}{4v_\beta^2\Gamma\omega}\left[\frac{\pi}{2} - \tan^{-1}\left(\frac{k_z^2v_\beta^2 - \omega^2}{2\Gamma\omega}\right)\right]. \tag{16}$$

Thus, the final form of $P_{\mathrm{BOLD}}(\omega)$ is

$$P_{\mathrm{BOLD}}(\omega) = \frac{1}{8\pi v_\beta^2\Gamma}\frac{P^2\omega^4 + (Q^2+2PR)\omega^2 + R^2}{\left[\left(-\omega^2 + \frac{1}{4}\kappa^2 + \omega_f^2\right)^2 + \kappa^2\omega^2\right][\omega^2 + (\eta+\tau^{-1})^2]}\frac{1}{\omega}\left[\frac{\pi}{2} - \tan^{-1}\left(\frac{k_z^2v_\beta^2 - \omega^2}{2\Gamma\omega}\right)\right]. \tag{17}$$

We can rewrite Eq. (17) in a compact form,

$$P_{\mathrm{BOLD}}(\omega) = \prod_{j=0}^{3} P_j(\omega), \tag{18}$$

where

$$P_0(\omega) = P^2\omega^4 + (Q^2+2PR)\omega^2 + R^2, \tag{19}$$

$$P_1(\omega) = \frac{1}{8\pi v_\beta^2\Gamma\omega}\left[\frac{\pi}{2} - \tan^{-1}\left(\frac{k_z^2v_\beta^2 - \omega^2}{2\Gamma\omega}\right)\right], \tag{20}$$

$$P_2(\omega) = \frac{1}{\left(-\omega^2 + \frac{1}{4}\kappa^2 + \omega_f^2\right)^2 + \kappa^2\omega^2}, \tag{21}$$

$$P_3(\omega) = \frac{1}{\omega^2 + (\eta+\tau^{-1})^2}. \tag{22}$$

Note that $P_0(\omega)$ is a monotonically increasing function, since $(Q^2 + 2PR) \geqslant 0$ for any combination of parameter values from Table I, that modulates the amplitude of $P_{\mathrm{BOLD}}(\omega)$. Moreover, the index j in Eq. (18) matches that in Eq. (2), so $P_1(\omega)$, $P_2(\omega)$, and $P_3(\omega)$ represent the power spectrum factors due to the damped-wave, local-oscillating, and local-decaying BOLD response modes, respectively. These modes dictate the fundamental patterns of oscillations of the BOLD signal, with structures that are independent of the stimulus [27]. They describe the physical propagating and nonpropagating components of BOLD more directly than common signal analysis methods such as independent component analysis. This is because such methods do not account for the nature of the system that produces the signals and are not based on brain physiology, so their results may mix the dynamics of fundamental brain modes. Hence, being able to separate the contributions of the modes to the BOLD power spectrum is a powerful feature of our formulation that is currently lacking in point models of hemodynamic responses.

B. Limiting behavior

To predict how the BOLD power spectrum and its factors behave, here we investigate their limiting behavior at low frequencies ($\omega \ll \omega_T$) and at high frequencies ($\omega \gg \omega_T$), where ω_T is a transition frequency. The transition frequency ω_T lies between the lowest and highest values of the natural frequencies of $P_{\mathrm{BOLD}}(\omega)$. From Eqs. (19)–(22), the natural

frequencies correspond to the model parameters that are in the set $S = \{\omega_f, \kappa, \eta, \tau, k_z v_\beta, \Gamma\}$ such that $\min(S) \leqslant \omega_T \leqslant \max(S)$.

For $\omega \ll \omega_T$, the low-frequency limits of the BOLD power spectrum factors, denoted as P_j^{L}, are

$$P_0^{\mathrm{L}} \approx R^2, \tag{23}$$

$$P_1^{\mathrm{L}} \approx \frac{1}{8\pi v_\beta^2 \Gamma \omega}\left[\frac{\pi}{2} - \left(\frac{\pi}{2} - \frac{2\Gamma\omega}{k_z^2 v_\beta^2}\right)\right] = \frac{1}{4\pi k_z^2 v_\beta^4}, \tag{24}$$

$$P_2^{\mathrm{L}} \approx \frac{1}{\left(\frac{1}{4}\kappa^2 + \omega_f^2\right)^2}, \tag{25}$$

$$P_3^{\mathrm{L}} \approx \frac{1}{(\eta + \tau^{-1})^2}. \tag{26}$$

Hence, the low-frequency limit of the BOLD power spectrum $P_{\mathrm{BOLD}}^{\mathrm{L}}$ is

$$P_{\mathrm{BOLD}}^{\mathrm{L}} \approx \frac{R^2}{4\pi k_z^2 v_\beta^4 \left(\frac{1}{4}\kappa^2 + \omega_f^2\right)^2 (\eta + \tau^{-1})^2}, \tag{27}$$

which corresponds to a flat spectrum. For $\omega \gg \omega_T$, the high-frequency limits of the BOLD power spectrum factors, denoted as P_j^{H}, are

$$P_0^{\mathrm{H}} \approx P^2 \omega^4, \tag{28}$$

$$P_1^{\mathrm{H}} \approx \frac{1}{8\pi v_\beta^2 \Gamma \omega}\left[\frac{\pi}{2} - \left(-\frac{\pi}{2} + \frac{2\Gamma}{\omega}\right)\right] = \frac{\pi\omega - 2\Gamma}{8\pi v_\beta^2 \Gamma \omega^2}$$

$$\approx \frac{1}{8 v_\beta^2 \Gamma \omega}, \tag{29}$$

$$P_2^{\mathrm{H}} \approx \frac{1}{\omega^4}, \tag{30}$$

$$P_3^{\mathrm{H}} \approx \frac{1}{\omega^2}. \tag{31}$$

Hence, the high-frequency limit of the BOLD power spectrum $P_{\mathrm{BOLD}}^{\mathrm{H}}$ is

$$P_{\mathrm{BOLD}}^{\mathrm{H}} \approx \frac{P^2}{8 v_\beta^2 \Gamma \omega^3}, \tag{32}$$

which is a power law that scales as ω^{-3}. The shapes of P_j^{L}, $P_{\mathrm{BOLD}}^{\mathrm{L}}$, P_j^{H}, and $P_{\mathrm{BOLD}}^{\mathrm{H}}$ and the value of ω_T for different parameter combinations are investigated in Sec. IV.

IV. EFFECTS OF DIFFERENT PARAMETERS ON THE POWER SPECTRUM

In Sec. III, the BOLD power spectrum, its power spectrum factors, and their respective limiting behaviors were analytically derived. To better understand how they behave as functions of frequency, here we explore the effects of varying the model's independent parameters.

From Table I, the set of independent parameters that can vary and can directly affect the BOLD power spectrum and its factors is $\Theta = \{\beta, \tau, \kappa, \omega_f, L, \nu_\beta, \Gamma\}$. All the other parameters are either fixed to their assumed values from the literature or can be derived from the independent parameters via the formulas shown in Table I.

In this section, three types of parameter sets are analyzed: (i) nominal parameters (Θ_{nom}), wherein we use experimental parameters for one subject [33]; (ii) varying parameters, wherein one parameter from Θ is varied to within its physiological range and the remaining parameters are taken from Θ_{nom}; and (iii) fitted parameters (Θ_{fit}), wherein the parameters are tuned to fit the empirical power spectrum data sets in Fig. 1 [16,22–24].

A. Nominal parameters

The power spectrum in Eq. (18) rests on biophysical parameters that can be fitted independently to reflect the physiology and hemodynamics of multiple regions of the brain. Previously, we fitted these parameters to the primary visual cortex of an individual subject performing fixation tasks that involve certain types of visual stimulus, i.e., three stationary isoeccentric rings, one ring that expanded in eccentricity through time, and one isopolar arc that expanded in eccentricity through time [27,30,37]. The values of these experimental parameters, herein termed the nominal parameters, are $\Theta_{\mathrm{nom}} = \{\beta = 3.2, \tau = 1\ \mathrm{s}, \kappa = 0.57\ \mathrm{s}^{-1}, \omega_f = 0.49\ \mathrm{s}^{-1}, L = 3 \times 10^{-3}\ \mathrm{m}, \nu_\beta = 2 \times 10^{-3}\ \mathrm{m\,s}^{-1}, \Gamma = 0.8\ \mathrm{s}^{-1}\}$.

To demonstrate that Θ_{nom} produces realistic BOLD responses, Fig. 4 shows the predicted BOLD response to an impulsive, point neural stimulus $\phi(\mathbf{r}, t) = \delta(\mathbf{r})\delta(t)$, where $\delta(\cdot)$ is the Dirac-delta function. For simplicity, only the variation of the BOLD response versus distance perpendicular to the centerline of the evoked neural response is shown in Fig. 4(a). The BOLD response has waves traveling in both directions from the center ($x = 0$) that extend to $x \approx \pm 5$ mm, resembling the experimental evoked activity in Ref. [30]. These propagating waves have also been observed in a number of other recent studies [41,42]. The dashed line in Fig. 4(a) marks the local response at $x = 0$, with its corresponding temporal profile shown in Fig. 4(b). The profile in Fig. 4(b) matches the temporal form of the local hemodynamic response function conventionally used in neuroimaging studies [35]. This shows that the model with nominal parameters Θ_{nom} reproduces experimentally found features of the BOLD response, including waves.

Using Θ_{nom}, we can obtain the nominal BOLD power spectrum and its factors as functions of $f = \omega/2\pi$ via Eqs. (18)–(22). In order to easily compare their spectral profiles, each power spectrum is normalized with respect to its total power, i.e., $P(\omega) = P(\omega)/\int P(\omega) d\omega$, as seen in Fig. 5.

We find that the nominal P_{BOLD} is flat at $f \lesssim 0.02$ Hz, has a weak resonance at $f \approx 0.075$ Hz (the approximate closed-form expression of this resonance frequency is further discussed in Sec. IV B) similarly to that found in Ref. [8], and then scales as f^{-3} at $f \gtrsim 0.1$ Hz. The limiting behavior at $f < 0.02$ Hz and $f > 0.1$ Hz are consistent with our calculations in Sec. III B. Note, however, that these results contradict findings in other studies claiming that P_{BOLD} has a pure power-law behavior in the entire low-frequency range $f < 0.2$ Hz [7,15–19]. The reason for this contradiction is discussed in Sec. IV C.

All the P_j are flat at $f \lesssim 0.02$ Hz, which is why P_{BOLD} is flat in this frequency range. This is consistent with our

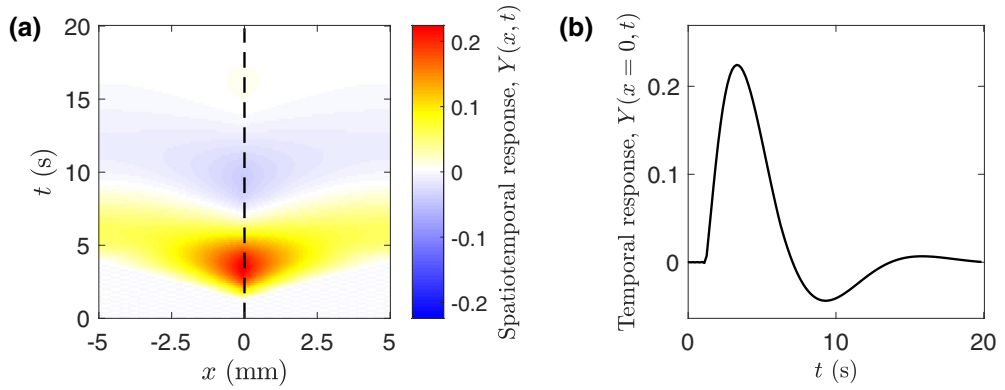

FIG. 4. Predicted BOLD response to an impulsive, point stimulus. (a) Spatiotemporal profile. The dashed line marks the response at $x = 0$. (b) Time profile at $x = 0$.

low-frequency limit calculations in Sec. III B. Then, the P_j's scale differently at high frequencies, with $P_0 \propto f^4$, $P_1 \propto f^{-1}$, $P_2 \propto f^{-4}$, and $P_3 \propto f^{-2}$, matching our high-frequency limit calculations in Sec. III B; this is why $P_{\mathrm{BOLD}} \propto f^{-3}$ at high frequencies. Finally, it is important to note that the weak resonance of P_{BOLD} depends strongly on P_0 and P_2. Hence, this suggests that we can better understand P_{BOLD}, including the existence of the resonance, by analyzing the properties of these BOLD power spectrum factors; this will be further explored in Sec. IV B.

The derived BOLD power spectrum can be further used to calculate the correlation function $C(t)$ of BOLD signal dynamics. We can easily calculate $C(t)$ by using the Wiener-Khintchine theorem, which states that the correlation function is equal to the inverse Fourier transform of the power spectrum. We then fit the results with an exponential function with a decay time of τ_s, which characterizes the intrinsic timescale of BOLD fluctuations. The resulting normalized correlation function $C(t)/C(t=0)$ and the corresponding exponential fit is shown in Fig. 6.

The resulting decay time is $\tau_s = 30.6 \pm 0.4$ s, which is close to the reported 34-s time lag that showed the strongest relationship between the topology of the structural connectome and spontaneous BOLD activity [59]. Moreover, this also agrees with the observed fluctuation scales of resting-state dynamic functional connectivity reported by recent studies [60–62]. This provides further evidence of the ability of the hemodynamic model to accurately describe the resting-state BOLD dynamics and implies that some changes in functional connectivity, defined via BOLD covariance, may reflect the BOLD correlation time, rather than alterations in the underlying structure.

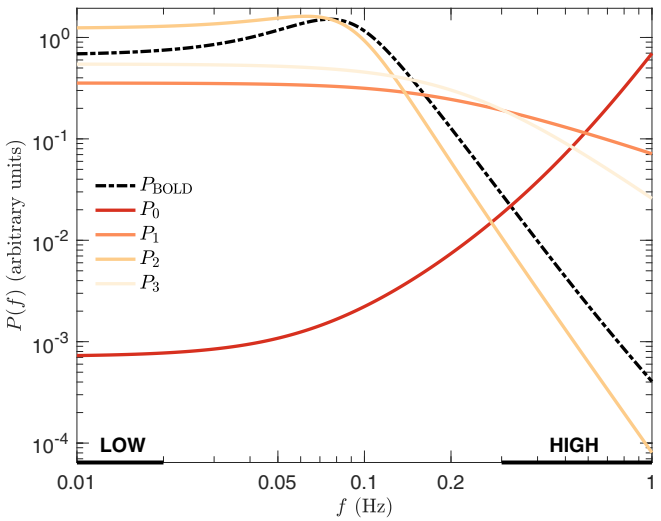

FIG. 5. Normalized theoretical BOLD power spectrum P_{BOLD} from Eq. (18) and its factors P_0–P_3 from Eqs. (19)–(22) using the nominal parameter set Θ_{nom} for $0.01\ \mathrm{Hz} \leqslant f \leqslant 1\ \mathrm{Hz}$. The curves are labeled according to the legend shown. The frequency ranges where the low- and high-frequency limit calculations in Sec. III B apply are highlighted by the black solid lines at the bottom of the frame.

B. Parameter sensitivities

Here, we explore the effects of varying the parameters of the analytic BOLD power spectrum and its factors. First, the independent parameters are initialized to their nominal values

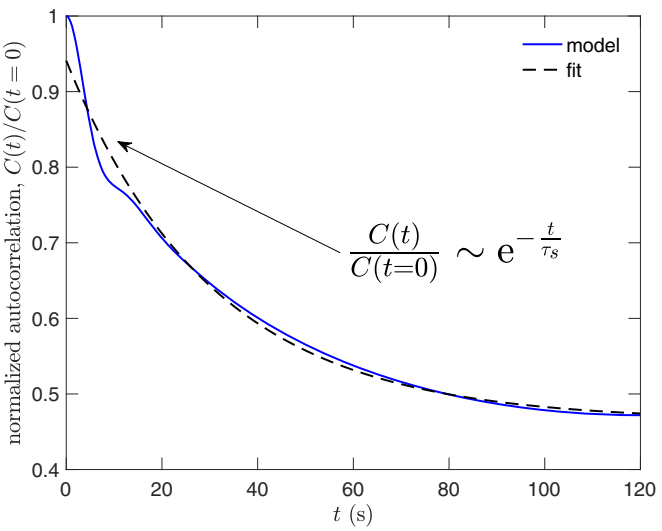

FIG. 6. Normalized BOLD correlation function $C(t)/C(t=0)$. The blue solid line represents the calculated correlation function, whereas the black dashed line represents the exponential fit with a decay time of $\tau_s = 30.6 \pm 0.4$ s ($r^2 = 0.99$).

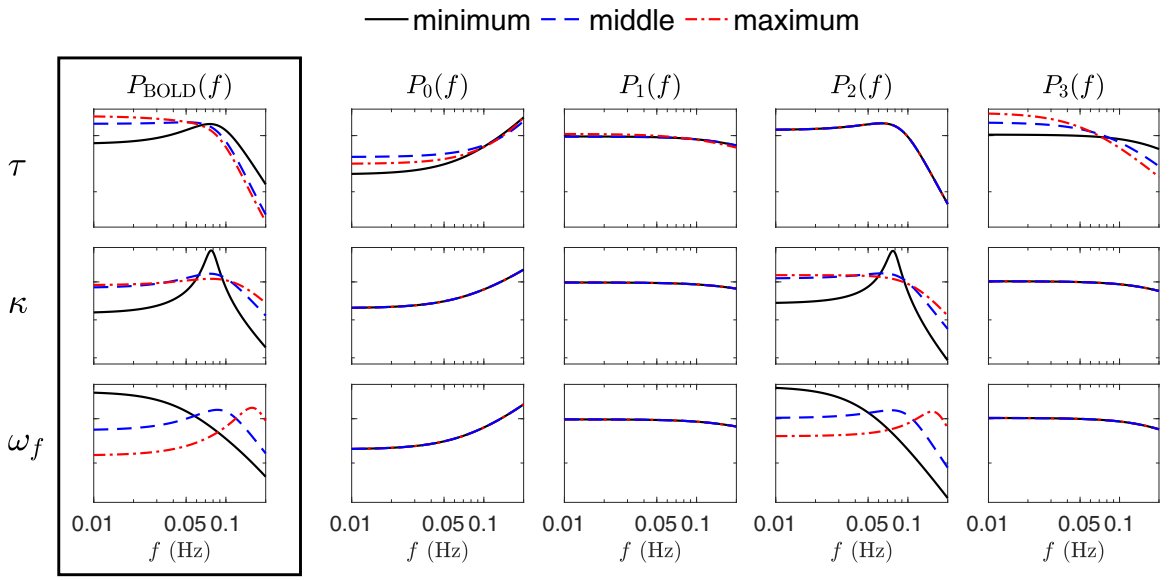

FIG. 7. Normalized theoretical power spectrum of BOLD P_{BOLD} and its factors P_0–P_3 using different parameter sets for 0.01 Hz $\leqslant f \leqslant$ 0.2 Hz. Columns from left to right show $P_{\mathrm{BOLD}}(f)$ (enclosed by a solid box), $P_0(f)$, $P_1(f)$, $P_2(f)$, and $P_3(f)$, respectively. Each row shows the profiles of the power spectra when one parameter (labeled on the left) is varied. The varied parameter uses its minimum (black solid line), middle (blue dashed line), or maximum (red dashed-dotted line) value from its physiological range in Table I. Note that a panel with only one visible curve indicates that the corresponding P_j does not depend on the parameter in question and follows its nominal profile from Fig. 5.

Θ_{nom}. Then, one parameter is varied across its physiological range defined in Table I; for brevity, we only show the normalized power spectrum profiles when the parameter is set to its minimum, middle, or maximum possible value. Moreover, our analysis reveals that only the temporal parameters τ, κ, and ω_f significantly affect the power spectrum profiles; hence Fig. 7 only shows their effects.

The following summarizes the results in Fig. 7, which are discussed by row of the figure:

(i) Changing τ does not affect P_2 and keeps its nominal profile, which is expected from its expression in Eq. (21). As τ increases toward its maximum value, P_0, P_1, P_3, and P_{BOLD} shift more of their energy to lower frequencies because higher τ means that blood takes longer to flow from large arteries to capillaries. In addition, the shape of P_{BOLD} is now strongly influenced by P_3, contrary to our previous observation for nominal parameters in Sec. IV A, and the resonance in P_{BOLD} disappears and is replaced by a knee. The knee frequency ω_{knee} for this case can be approximated by finding the frequency where the low- and high-frequency limits of P_3 intersect, i.e., where $P_3^{\mathrm{L}}(\omega_{\mathrm{knee}}) = P_3^{\mathrm{H}}(\omega_{\mathrm{knee}})$, yielding $\omega_{\mathrm{knee}} = \eta + \tau^{-1}$; hence, higher τ values lead to lower knee frequencies.

(ii) Changing the blood flow response parameters κ or ω_f does not affect P_0, P_1, and P_3, which is expected from Eqs. (19), (20), and (22), respectively. Moreover, the shape of P_{BOLD} is strongly influenced by P_2 with both having the same profile.

(iii) As κ decreases toward its minimum value, the resonance of P_{BOLD} gets stronger and the resonance frequency decreases minutely. The resonance frequency can be calculated by differentiating Eq. (21) to find the maximum of P_2, yielding

$$\omega_{\mathrm{res}} = \sqrt{\omega_f^2 - \tfrac{1}{4}\kappa^2}. \tag{33}$$

Hence, lower κ values lead to higher resonance frequencies. Equation (33) can be used to find the resonance frequency for any parameter combination. Note, however, that the resonance disappears when $\omega_f \leqslant \frac{1}{2}\kappa$, as seen from the red dashed-dotted curves of P_{BOLD} and P_2 in Fig. 7, row 2, where κ is maximal.

(iv) As ω_f decreases toward its minimum value, the relative powers of P_2 and P_{BOLD} at $f \lesssim 0.05$ Hz increase and the resonance disappears, which happens because $\omega_f < \frac{1}{2}\kappa$; the resonance changes to a knee. However, the knee frequency previously derived for varying τ needs to be changed to the frequency where the low- and high-frequency limits of P_2 intersect, i.e., where $P_2^{\mathrm{L}}(\omega_{\mathrm{knee}}) = P_2^{\mathrm{H}}(\omega_{\mathrm{knee}})$, yielding

$$\omega_{\mathrm{knee}} = \sqrt{\omega_f^2 + \tfrac{1}{4}\kappa^2}. \tag{34}$$

C. Fitted parameters

Our parameter sensitivity exploration in Sec. IV B implies that physiological parameters strongly influence the overall shape of P_{BOLD}. Hence, in this section, we investigate whether a parameter set Θ_{fit} exists that can fit the theoretical P_{BOLD} to findings in the literature, specifically the empirical data sets in Fig. 1 [16,22–24].

First, the independent parameters are initialized to their nominal values Θ_{fit}. Then, τ, ω_f, and κ are varied to fit the resulting theoretical P_{BOLD} with the empirical data sets in Fig. 1. Nonlinear least-squares fitting is used to estimate the best-fit parameters Θ_{fit} that minimize the residual sum of squares between the model and the data on a log-log scale; the results are shown in Table II. Note that the fits are also constrained by limiting the fitted parameters within their physiological bounds shown in Table I. The fitted theoretical BOLD power spectra superimposed on the corresponding empirical data are shown in Fig. 8.

TABLE II. Best-fit parameters for the empirical data sets in Fig. 1 [16,22–24].

	$\boldsymbol{\Theta}_{\text{fit}}$		
Data sets	τ (s)	κ (s^{-1})	ω_f (s^{-1})
He *et al.* [16]	1.1	0.8	0.2
Boynton *et al.* [22]	1.8	1.0	0.4
Bandettini [23]	1.4	0.8	0.4

Figure 8(a) shows that the model produces a flat spectrum at $f \lesssim 0.01$ Hz and a power law at $f \gtrsim 0.06$ Hz. This onset frequency matches the data in Ref. [16] but the asymptotic power-law exponent of the model is 3 [which is that found in Eq. (32) for any parameter combination], whereas the data have an asymptotic power-law exponent of 0.87 ± 0.03. Figure 8(b) shows that the model produces a flat spectrum at $f \lesssim 0.02$ Hz and a power law at $f \gtrsim 0.07$ Hz. Similarly to Fig. 8(a), the model accurately captures the onset frequency that separates the flat spectrum from a power law exhibited by the data in Refs. [22,24] but the asymptotic power-law exponents are different, i.e., 3 for the model versus 1.20 ± 0.03 for the data. Finally, Fig. 8(c) shows that the model produces a power spectrum that matches the data in Refs. [23,24], i.e., a flat spectrum at $f \lesssim 0.04$ Hz and a power law at $f \gtrsim 0.08$ Hz having an asymptotic exponent of 3 for the model and 2.88 ± 0.06 for the data.

These results yield the following key findings:

(i) Our theoretical work implies that low-frequency BOLD for all realistic parameter combinations has a flat spectrum at $f \lesssim 0.01$ Hz, which makes sense physically because a power law would diverge as $f \to 0$. This is consistent with the results in Refs. [22–24] and with experimental and theoretical findings showing that the underlying resting-state neural activity in this frequency range, which BOLD is most sensitive to, has a flat spectrum [53–55]. However, this result is contrary to that claimed in Ref. [16] that BOLD exhibits a pure power-law spectrum in this frequency range. This is an important aspect of BOLD dynamics that is often not discussed in the current literature, which may be attributed to limitations in experimental paradigms that prevent the acquisition of highly resolved data because the duration of current protocols is too short to be able to investigate frequencies $\lesssim$0.01 Hz. In signal processing, the frequency bandwidth (Δf) and time duration (Δt) of a signal are physically constrained by $\Delta f \Delta t > 1$; hence, to be able to investigate BOLD at frequencies $<$0.01 Hz, the duration of the protocol must be at least 100 s, which is larger than typical experimental protocols.

(ii) Our work predicts a knee that separates the flat spectrum from a power law at higher frequencies. This knee was argued in Ref. [8] but was not mentioned in Refs. [16,22] even though their data clearly show it. For example, the analysis in Ref. [16] disregarded that the first few data points resemble a flat spectrum and reported that the spectrum follows a consistent power-law behavior. Features of the BOLD spectrum, such as the knee, are often difficult to account for in experimental studies because of insufficient frequency resolution in the low-frequency regime, but are important to accurately describe BOLD dynamics.

(iii) The model power spectrum demonstrates a power law at $f \gtrsim 0.06$ Hz that has a significantly different exponent than those found in Refs. [16,22] but matches the data for a single subject and brain region in Ref. [23]. A possible explanation for this discrepancy is that many current fMRI spectral studies present a BOLD power spectrum that has been obtained by averaging data to increase the signal-to-noise ratio. This involves either averaging the BOLD time series via smoothing operations and filters or averaging the spectra in frequency space. Furthermore, data could be averaged from multiple voxels to represent the general characteristics of a region of interest or from multiple subjects to represent group statistics. Since different voxels and subjects naturally exhibit unique cortical properties, the process of averaging removes intrinsic variability and smears out important features of the BOLD power spectrum, such as the transition frequency ω_T, discussed in Sec. III. In addition, averaging spectra with different knees and high-frequency power-law exponents can

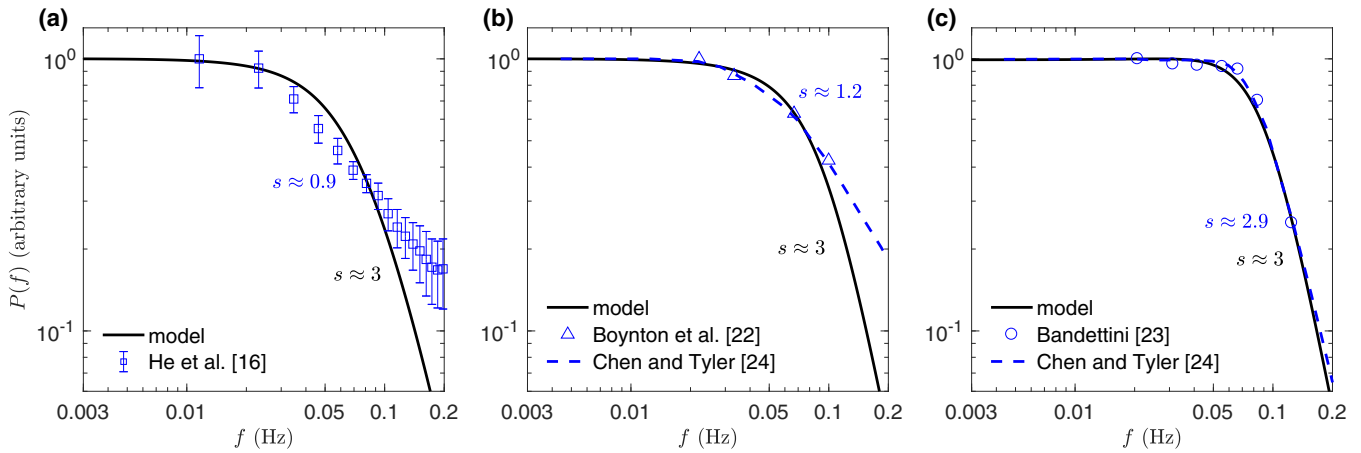

FIG. 8. Comparison of BOLD power spectrum from the model and various empirical data sets. (a) Model (black solid line) vs Ref. [16] (blue squares: mean; error bar: one standard deviation) data described in Fig. 1(a). (b) Model (black solid line) vs Ref. [22] (blue triangles) and Ref. [24] (blue dashed line) data described in Fig. 1(b). (c) Model (black solid line) vs Ref. [23] (blue circles) and Ref. [24] (blue dashed line) data described in Fig. 1(b). For each panel, the approximate power-law exponents (s) of the asymptotic curves are shown.

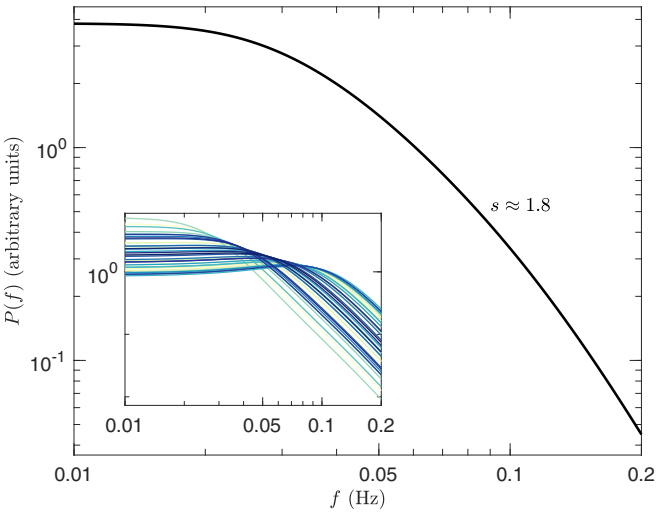

FIG. 9. Effect of data averaging on the BOLD power spectrum. The main panel shows the mean power spectrum and the approximate asymptotic power-law exponent, whereas the inset shows the 40 individual power spectra that were averaged to produce the main curve.

also strongly bias the resulting curve's high-frequency power-law exponent toward lower values, yielding exponents that are completely different from those of the individual spectra. This argument is supported by Fig. 8(c), wherein the model matches the shape, the location of the knee, and the high-frequency power-law exponent of the spectrum for one subject and brain region without averaging; these points are explored further in the next section.

V. IMPACT OF DATA AVERAGING

We demonstrate the impact of data averaging by simulating individual spectra obtained by using different parameter sets. For illustration purposes, we use the parameter set $\Theta_{\rm nom}$ and randomly vary the parameter ω_f within its physiological range shown in Table I to generate 40 different spectra. The results are shown in Fig. 9 with the average shown in the main panel and the individual power spectra shown in the inset.

The individual spectra have different transition frequencies ω_T, with some having a weak resonance and some having increased power at $f \lesssim 0.01$ Hz, but all have asymptotic power-law exponents of 3. Averaging them gives a mean spectrum with features that are significantly different from the individual power spectra; in particular, the asymptotic power-law exponent decreases from 3 to 1.8. Hence, if more individual spectra are considered in the data averaging process, asymptotic power-law exponents closer to estimates in Ref. [16] are possible. This issue of data averaging to show evidence for a power-law spectrum is prevalent in the general literature (e.g., Refs. [25,63]), and our study clearly demonstrates that this must be carefully considered in the context of BOLD spectral analysis.

VI. EFFECT OF ASSUMED NOISE SPECTRUM

One of the assumptions of the study is that resting-state neural activity can be approximated as a white noise with a constant power spectrum throughout the frequency bandwidth of BOLD. This is based on studies showing that fluctuations in the resting-state BOLD signal are positively correlated with low-frequency EEG power [51,52], which is approximately flat at $f < 1$ Hz [53–55] where BOLD is most sensitive. However, other works have shown that long-duration EEG time series (which affects low-frequency dynamics) and underlying neuronal fluctuations could exhibit power-law scaling at $f > 0.5$ Hz [64–66]. Hence, a power-law form for the spectral profile of the noise spectrum could be considered.

We test this by generating noise spectra with a power-law form of $P(f) \propto f^{\gamma}$, where γ is the scaling exponent, and compare the resulting BOLD spectrum. For demonstration purposes, we use four typical noise spectra found in the literature with (i) $\gamma = 0$ for white noise, (ii) $\gamma = -1$ for pink noise, (iii) $\gamma = -2$ for brown noise, and (iv) $\gamma = 1$ for blue noise. The normalized noise spectra are shown in Fig. 10(a), and the resulting normalized BOLD spectra obtained from the product of Eq. (18) with the noise spectra are shown in Fig. 10(b).

It is clear from Fig. 10 that when $\gamma < 0$, the asymptotic power-law exponent of the BOLD spectrum only becomes steeper and deviates further from the estimates in Ref. [16]. Moreover, these noise spectra cannot extend to $f = 0$ and must always level off to avoid divergence of their total power. On the other hand, $\gamma > 0$ brings the asymptotic power-law exponent closer to estimates in Ref. [16]; however, there is a significant decrease in the power at $f \lesssim 0.01$ Hz that is not seen in the data. These results provide evidence that a power-law noise spectrum is not a viable solution to reconcile the discrepancy between our theoretical predictions and empirical data in Refs. [16,22]. Hence, we conclude from these comparisons that the ansatz of a white noise spectrum is appropriate and that the reduction of the discrepancy is more likely due to effects such as that of data averaging, as discussed in the previous section.

VII. SUMMARY AND DISCUSSION

Here, we have used an experimentally verified physiological cortical hemodynamic model, which can accurately represent the properties of the cortex and can predict the BOLD signal via its hemodynamic mechanisms, to analytically derive the power spectrum of the resting-state BOLD response. We examined how the model's parameters affect the BOLD power spectrum and its individual spectral factors, giving important insights into its spectral characteristics in comparison with empirical data.

Our calculations show that for nominal parameters, the BOLD power spectrum is flat at $f \lesssim 0.02$ Hz, exhibits a weak resonance, and then scales as f^{-3} at $f \gtrsim 0.1$ Hz. In addition, the correlation function derived from the power spectrum showed an intrinsic timescale similar to that found for spontaneous BOLD activity and dynamic functional connectivity. We also investigated the effects of varying model parameters on the profile of the BOLD power spectrum and its factors and showed that parameters related to the hemodynamic transit time and blood flow response properties strongly influence the amplitude and frequency of BOLD's resonance.

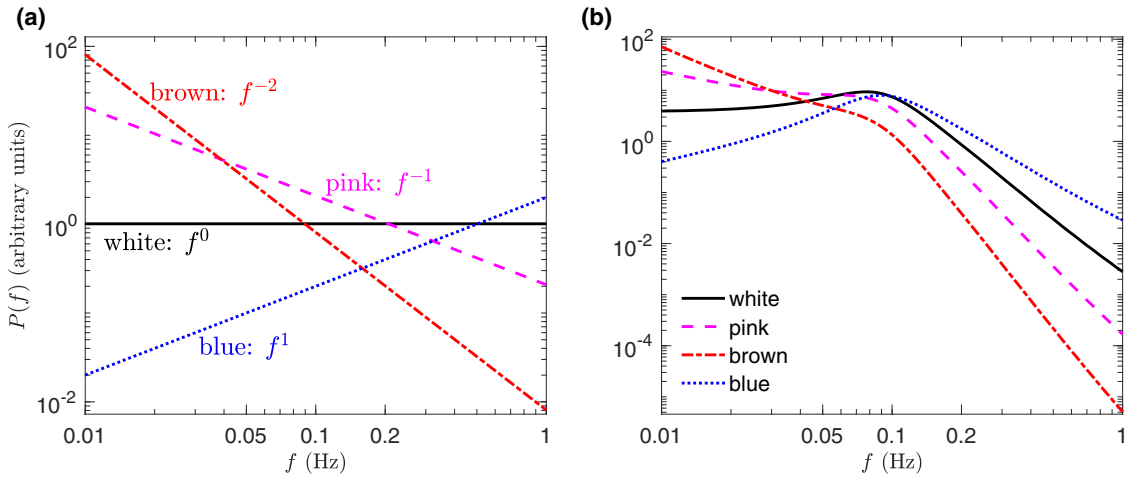

FIG. 10. Effect of using noise spectra with power-law forms. (a) Noise spectrum. The labels show the type of noise used and the corresponding equation of $P(f)$. (b) Resulting BOLD spectrum. The curves are labeled according to the legend shown.

Finally, we tuned the model parameters to fit the analytic BOLD power spectrum to empirical data sets. We found that the spectrum remains flat at the ultralow-frequency range ($f < 0.01$ Hz) for all parameter combinations, agreeing with the results in Refs. [22–24] and with findings that the underlying resting-state neural activity in this frequency range has a flat spectrum. Our fits also reveal that the empirical data exhibit a knee that separates the flat spectrum from a power law at high frequencies, which are not mentioned in experimental studies even though the data clearly show it because of insufficient frequency resolution. We also found that the model spectrum demonstrates a power law for high frequencies that has a significantly different exponent than those found in Refs. [16,22] but matches the data for a single subject and brain region in Ref. [23].

We demonstrated via an illustrative example that the discrepancy between our theory and data can be plausibly attributed chiefly to data averaging performed by experimental studies that aim to increase the signal-to-noise ratio. We showed that averaging removes the intrinsic variability of brain regions and subjects that biases the resulting curve's power-law exponent; indeed, averaging reduced the model's predicted asymptotic power-law exponent of 3 to 1.8, suggesting that data averaging must be carefully considered to obtain an accurate description of the BOLD spectral properties. In fact, the data in Ref. [23] support this argument, wherein the model matches the shape, the location of the knee, and the high-frequency power-law exponent of the spectrum for data from one subject and brain region in the absence of averaging. We also demonstrated that changing the noise spectrum from white to a power-law form of f^γ with $\gamma \neq 0$ only worsens the agreement between our theory and data. Other structured noise can be studied in the future using our approach.

Even with the strong arguments laid down in favor of our formulations and analyses, another potential reason for the inconsistency between our theory and data, aside from the data averaging effect mentioned above, is that we considered fMRI time series to be driven purely by neural activity without incorporating instrumental or other noise and that the transfer function in Eq. (2) is sufficient to model this. It is possible that other nonphysiological components and/or noise, e.g., thermal noise, could mix with neural activity to interfere with the measurement of the underlying BOLD power spectrum. This can be potentially addressed by combining our formulations with dynamic causal modeling (DCM) [47]. DCM allows inference of the possible models of the underlying causal architecture of coupled dynamic systems. It has recently been extended for use with resting-state fMRI [58,67,68], and can accommodate neuronal fluctuations and the contribution of other stochastic effects.

Overall, this study demonstrates the ability of our hemodynamic model to produce voxel- or subject-specific noise-free dynamics of BOLD and further analyze its low-frequency behavior, going beyond the limitations and existing issues of current fMRI spectral studies. It also uses the model to explain the impact of *ad hoc* data processing, such as data averaging, and other noise spectra on the reported features of the BOLD power spectrum. This is the advantage of a theoretical study such as ours because several hypotheses can be directly tested and be confirmed or rejected.

ACKNOWLEDGMENTS

This work was supported by the Australian Research Council Center of Excellence for Integrative Brain Function (ARC Center of Excellence Grant No. CE140100007), the Australian Research Council Laureate Fellowship Grant No. FL140100025, and the Australian Research Council Discovery Project Grant No. DP170101778.

[1] N. K. Logothetis, Nature (London) **453**, 869 (2008).
[2] P. A. Bandettini, NeuroImage **62**, 575 (2012).
[3] B. Biswal, F. Z. Yetkin, V. M. Haughton, and J. S. Hyde, Magn. Reson. Med. **34**, 537 (1995).

[4] M. D. Fox and M. E. Raichle, Nat. Rev. Neurosci. **8**, 700 (2007).
[5] J. D. Power, B. L. Schlaggar, and S. E. Petersen, Neuron **84**, 681 (2014).
[6] J.-S. Park, J. Seo, H. Cha, H.-J. Song, S.-H. Lee, K. E. Jang, H. J. Lee, J. Park, H.-W. Lee, and Y. Chang, Sci. Rep. **8**, 987 (2018).
[7] E. Zarahn, G. K. Aguirre, and M. D'Esposito, NeuroImage **5**, 179 (1997).
[8] P. A. Robinson, P. M. Drysdale, H. Van der Merwe, E. Kyriakou, M. K. Rigozzi, B. Germanoska, and C. J. Rennie, NeuroImage **31**, 585 (2006).
[9] E. D. Duff, L. A. Johnston, J. Xiong, P. T. Fox, I. Mareels, and G. F. Egan, Hum. Brain Mapp. **29**, 778 (2008).
[10] B. L. Foster, B. J. He, C. J. Honey, K. Jerbi, A. Maier, and Y. B. Saalmann, Front. Syst. Neurosci. **10**, 7 (2016).
[11] P. P. Mitra, S. Ogawa, X. Hu, and K. Uğurbil, Magn. Reson. Med. **37**, 511 (1997).
[12] R. G. Wise, K. Ide, M. J. Poulin, and I. Tracey, NeuroImage **21**, 1652 (2004).
[13] Y. He, M. Wang, X. Chen, R. Pohmanna, J. R. Polimeni, K. Scheffler, B. R. Rosen, D. Kleinfeld, and X. Yu, Neuron **97**, 925 (2018).
[14] P. Bak, *How Nature Works: The Science of Self-Organized Criticality* (Copernicus, New York, 1996).
[15] M. D. Fox, A. Z. Snyder, J. L. Vincent, and M. E. Raichle, Neuron **56**, 171 (2007).
[16] B. J. He, J. M. Zempel, A. Z. Snyder, and M. E. Raichle, Neuron **66**, 353 (2010).
[17] B. J. He, J. Neurosci. **31**, 13786 (2011).
[18] B. J. He, Trends Cogn. Sci. **18**, 480 (2014).
[19] M. Kasagi, Z. Huang, K. Narita, H. Shitara, T. Motegi, Y. Suzuki, K. Fujihara, S. Tanabe, H. Kosaka, K. Ujita, M. Fukuda, and G. Northoff, Behav. Neurol. **2017**, 2824615 (2017).
[20] A. Eke, P. Herman, L. Kocsis, and L. R. Kozak, Physiol. Meas. **23**, R1 (2002).
[21] P. Berkes, G. Orbán, M. Lengyel, and J. Fiser, Science **331**, 83 (2011).
[22] G. M. Boynton, S. A. Engel, G. H. Glover, and D. J. Heeger, J. Neurosci. **16**, 4207 (1996).
[23] P. A. Bandettini, in *Functional MRI*, edited by C. T. W. Moonen and P. A. Bandettini (Springer, Berlin, 1999), pp. 205–220.
[24] C. C. Chen and C. W. Tyler, in *Novel Trends in Brain Science*, edited by M. Onozuka and C.-T. Yen (Springer, Tokyo, 2008), pp. 63–76.
[25] A. Clauset, C. R. Shalizi, and M. E. J. Newman, SIAM Rev. **51**, 661 (2009).
[26] M. Newman, Significance **14**, 10 (2017).
[27] J. C. Pang, P. A. Robinson, and K. M. Aquino, J. R. Soc. Interface **13**, 20160253 (2016).
[28] T. T. Liu, NeuroImage **143**, 141 (2016).
[29] P. M. Drysdale, J. P. Huber, P. A. Robinson, and K. M. Aquino, J. Theor. Biol. **265**, 524 (2010).
[30] K. M. Aquino, M. M. Schira, P. A. Robinson, P. M. Drysdale, and M. J. Breakspear, PLoS Comput. Biol. **8**, e1002435 (2012).
[31] K. M. Aquino, P. A. Robinson, and P. M. Drysdale, J. Theor. Biol. **347**, 118 (2014).
[32] J. C. Pang, P. A. Robinson, K. M. Aquino, and N. Vasan, NeuroImage **147**, 994 (2017).
[33] J. C. Pang, K. M. Aquino, P. A. Robinson, T. C. Lacy, and M. M. Schira, J. Neurosci. Methods **308**, 6 (2018).
[34] H. M. Duvernoy, S. Delon, and J. L. Vannson, Brain Res. Bull. **7**, 519 (1981).
[35] K. J. Friston, A. Mechelli, R. Turner, and C. J. Price, NeuroImage **12**, 466 (2000).
[36] K. E. Stephan, N. Weiskopf, P. M. Drysdale, P. A. Robinson, and K. J. Friston, NeuroImage **38**, 387 (2007).
[37] T. C. Lacy, K. M. Aquino, P. A. Robinson, and M. M. Schira, J. R. Soc. Interface **13**, 20160576 (2016).
[38] A. M. Puckett, K. M. Aquino, P. A. Robinson, M. J. Breakspear, and M. M. Schira, NeuroImage **139**, 240 (2016).
[39] Y.-R. Gao, S. E. Greene, and P. J. Drew, NeuroImage **115**, 162 (2015).
[40] N. Gravel, R. J. Renken, B. M. Harvey, G. Deco, F. W. Cornelissen, and M. Gilson, bioRxiv 172452 (2017).
[41] L. Muller, F. Chavane, J. Reynolds, and T. J. Sejnowski, Nat. Rev. Neurosci. **19**, 255 (2018).
[42] A. Shatillo, A. Lipponen, R. A. Salo, H. Tanila, A. Verkhratsky, R. Giniatullin, and O. H. Gröhn, J. Cereb. Blood Flow Metab., (2018), doi:10.1177/0271678X18772994.
[43] K. M. Aquino, P. A. Robinson, M. M. Schira, and M. J. Breakspear, NeuroImage **94**, 203 (2014).
[44] A. Gaglianese, M. J. Vansteensel, B. M. Harvey, S. O. Dumoulin, N. Petridou, and N. F. Ramsey, NeuroImage **155**, 480 (2017).
[45] R. J. Trudnowski and R. C. Rico, Clin. Chem. **20**, 615 (1974).
[46] B. Fischl and A. M. Dale, Proc. Natl. Acad. Sci. USA **97**, 11050 (2000).
[47] K. J. Friston, L. Harrison, and W. Penny, NeuroImage **19**, 1273 (2003).
[48] R. B. Buxton, K. Uludağ, D. J. Dubowitz, and T. T. Liu, NeuroImage **23**, S220 (2004).
[49] T. J. Huppert, R. D. Hoge, S. G. Diamond, M. A. Franceschini, and D. A. Boas, NeuroImage **29**, 368 (2006).
[50] D. A. Boas and S. J. Payne, Physiol. Meas. **30**, L9 (2009).
[51] H. Lu, Y. Zuo, H. Gu, J. A. Waltz, W. Zhan, C. A. Scholl, W. Rea, Y. Yang, and E. A. Stein, Proc. Natl. Acad. Sci. USA **104**, 18265 (2007).
[52] G. V. Portnova, A. Tetereva, V. Balaev, M. Atanov, L. Skiteva, V. Ushakov, A. Ivanitsky, and O. Martynova, Front. Hum. Neurosci. **11**, 654 (2018).
[53] P. A. Robinson, C. J. Rennie, J. J. Wright, H. Bahramali, E. Gordon, and D. L. Rowe, Phys. Rev. E **63**, 021903 (2001).
[54] R. G. Abeysuriya, C. J. Rennie, and P. A. Robinson, J. Neurosci. Methods **253**, 55 (2015).
[55] J. C. Pang and P. A. Robinson, NeuroImage **181**, 461 (2018).
[56] P. A. Robinson, C. J. Rennie, D. L. Rowe, and S. C. O'Connor, Hum. Brain Mapp. **23**, 53 (2004).
[57] O. David and K. J. Friston, NeuroImage **20**, 1743 (2003).
[58] A. Razi, J. Kahan, G. Rees, and K. J. Friston, NeuroImage **106**, 1 (2015).
[59] S. S. Sethi, V. Zerbi, N. Wenderoth, A. Fornito, and B. D. Fulcher, Chaos **27**, 047405 (2017).
[60] E. A. Allen, E. Damaraju, S. M. Plis, E. B. Erhardt, T. Eichele, and V. D. Calhoun, Cereb. Cortex **24**, 663 (2014).
[61] A. Zalesky, A. Fornito, L. Cocchi, L. L. Gollo, and M. Breakspear, Proc. Natl. Acad. Sci. USA **111**, 10341 (2014).
[62] R. F. Betzel, M. Fukushima, Y. He, X.-N. Zuo, and O. Sporns, NeuroImage **127**, 287 (2016).
[63] A. Heathcote, S. Brown, and D. J. K. Mewhort, Psychon. Bull. Rev. **7**, 185 (2000).

[64] C. W. Shin and S. Kim, Phys. Rev. E **74**, 045101(R) (2006).
[65] P. Allegrini, P. Paradisi, D. Menicucci, and A. Gemignani, Front. Physiol. **1**, 128 (2010).
[66] J. W. Kantelhardt, S. Tismer, F. Gans, A. Y. Schumann, and T. Penzel, Europhys. Lett. **112**, 18001 (2015).
[67] K. J. Friston, J. Kahan, B. Biswal, and A. Razi, NeuroImage **94**, 396 (2014).
[68] A. Razi, M. L. Seghier, Y. Zhou, P. McColgan, P. Zeidman, H.-J. Park, O. Sporns, G. Rees, and K. J. Friston, Network Neurosci. **1**, 222 (2017).